The Astrophysical Journal, 863:98 (15pp), 2018 August 10 https://doi.org/10.3847/1538-4357/aad1f0

Leptonic and Hadronic Modeling of *Fermi*-LAT Hard Spectrum Quasars and Predictions for High-energy Polarization

Vaidehi S. Paliya[1], Haocheng Zhang[2], Markus Böttcher[3], M. Ajello[1], A. Domínguez[4], M. Joshi[5], D. Hartmann[1], and C. S. Stalin[6]
[1] Department of Physics and Astronomy, Clemson University, Kinard Lab of Physics, Clemson, SC 29634-0978, USA; vpaliya@g.clemson.edu
[2] Department of Physics and Astronomy, Purdue University, West Lafayette, IN 47907, USA
[3] Centre for Space Research, North-West University, Potchefstroom, 2520, South Africa
[4] 3Grupo de Altas Energías, Universidad Complutense, E-28040 Madrid, Spain
[5] Institute for Astrophysical Research, Boston University, 725 Commonwealth Avenue, Boston, MA 02215, USA
[6] Indian Institute of Astrophysics, Block II, Koramangala, Bangalore-560034, India
Received 2018 January 25; revised 2018 June 27; accepted 2018 July 4; published 2018 August 14

Abstract

We present the results of a study of the time-averaged spectral energy distributions (SEDs) of eight flat spectrum radio quasars (FSRQs) present in the second catalog of high energy sources detected beyond 50 GeV by the *Fermi* Large Area Telescope (2FHL). Both leptonic and hadronic scenarios are adopted to explain the multiwavelength SEDs and we find them to be marginally consistent with the 2FHL spectra above 50 GeV. We derive the expected degree of X-ray and γ-ray polarizations both for the average and elevated activity states and note that (i) a hadronic radiative model consistently predicts a higher degree of high energy polarization compared to leptonic ones and (ii) the X-ray polarization degree is higher than the γ-ray polarization in the leptonic scenario, but similar to the γ-ray polarization if the observed radiation is powered by hadronic processes. From the leptonic modeling, the location of the γ-ray emitting region is found to be at the outer edge of the broad line region (BLR) and is consistent with the $\gamma\gamma$ opacity estimates for the γ-ray absorption by the BLR. We conclude that a majority of the FSRQs could be detected by the upcoming Cherenkov Telescope Array, though future high energy polarimeters will be able to detect them only during elevated activity states, which could provide supportive evidence for the hadronic origin of the X-ray and γ-ray emission.

Key words: galaxies: active – galaxies: jets – gamma rays: galaxies – radiation mechanisms: non-thermal

1. Introduction

Blazars are radio-loud active galactic nuclei (AGNs) with their relativistic jets pointed toward the observer (Urry & Padovani 1995). Due to the peculiar orientation of the jet, the flux across the electromagnetic spectrum, from radio waves to very high energy (VHE) γ-rays, is strongly enhanced by relativistic Doppler boosting. Blazars are subdivided into two categories, flat spectrum radio quasars (FSRQs) and BL Lac objects, with FSRQs exhibiting broad emission lines (equivalent width >5 Å). The observation of strong optical–UV emission lines from FSRQs indicates the presence of a luminous broad line region (BLR), which, in turn, suggests an efficient accretion process illuminating it (e.g., Sbarrato et al. 2012).

The spectral energy distribution (SED) of blazars consists of two broad nonthermal components. The low-energy (radio to UV/X-ray) component in the blazar SED is understood to originate from synchrotron emission by electrons in the relativistic jet. However, the origin of the high-energy SED component from X-rays to γ-rays is less understood. In the leptonic emission scenario, the high energy radiation is produced via inverse Compton (IC) scattering of low-energy photon fields that can be either synchrotron emission (synchrotron self-Compton or SSC; e.g., Marscher & Gear 1985) or can originate outside the jet (External Compton or EC; e.g., Begelman & Sikora 1987). Accordingly, in the canonical picture of the powerful FSRQs, it is assumed that the primary site of the γ-ray emission lies inside the BLR or outside the BLR but inside the torus, where intense radiation fields from the BLR and torus provide seed photons for the IC mechanism (e.g., Ghisellini & Tavecchio 2009). Alternatively, the hadronic scenario suggests that both primary electrons and protons are accelerated to ultrarelativistic energies. Here, the high-energy emission is dominated by synchrotron emission of primary protons and secondary particles in electromagnetic cascades initiated by photon-pion and photo-pair production (Mannheim & Biermann 1992; Aharonian 2000; Mücke & Protheroe 2001; Böttcher et al. 2013).

Both leptonic and hadronic scenarios have been successful in reproducing the steady-state spectra of blazars (Böttcher et al. 2013). However, they require very different jet energetics and particle dynamics. Interestingly, Zhang & Böttcher (2013) have shown that the high-energy polarization signatures can be dramatically different in these two scenarios. This is because, in general, the relativistic Compton scattering that dominates the high-energy emission in the leptonic model generally produces lower polarization degrees than the proton and cascade synchrotron emission in the hadronic model. Thus, X-ray and γ-ray polarization signatures can be used to distinguish the origin of the high-energy emission from FSRQs, making them promising targets for the future X-ray polarimeters (e.g., IXPE; Weisskopf et al. 2016).

Abdo et al. (2010) have classified blazars based on the location of the synchrotron peak in their SEDs. A source is defined as low synchrotron peaked (LSP) if the rest-frame synchrotron peak frequency ($\nu_{\rm syn}^{\rm peak}$) is less than 10^{14} Hz. On the other hand, in the case of $10^{14}\,{\rm Hz} < \nu_{\rm syn}^{\rm peak} < 10^{15}$ Hz and $\nu_{\rm syn}^{\rm peak} > 10^{15}$ Hz, blazars are classified as intermediate synchrotron peaked and high synchrotron peaked objects, respectively. In general, FSRQs are LSP sources and

Table 1
Basic 2FHL Properties of the Gamma-Ray Blazars Studied in This Work

2FHL Name (1)	Other Name (2)	z (3)	TS (4)	$F_{0.05-2\,\mathrm{TeV}}$ (5)	$\Gamma_{0.05-2\,\mathrm{TeV}}$ (6)	N_{pred} (7)	3FGL (8)
J0456.9−2323	PKS 0454−234	1.00	30.7	1.53 ± 0.78	3.23 ± 1.16	4.1	J0457.0−2324
J0957.6+5523	4C +55.17	0.90	120.3	3.59 ± 1.03	3.49 ± 0.72	12.9	J0957.6+5523
J1224.7+2124	4C +21.35	0.43	108.0	5.44 ± 1.29	4.06 ± 0.74	15.0	J1224.9+2122
J1256.2−0548	3C 279	0.54	47.4	1.87 ± 0.87	4.44 ± 1.61	4.9	J1256.1−0547
J1427.3−4204	PKS B1424−418	1.55	41.8	1.65 ± 0.74	11.30 ± 4.60	5.0	J1427.9−4206
J1512.7−0906	PKS 1510−08	0.36	124.0	4.59 ± 1.28	2.99 ± 0.57	13.1	J1512.8−0906
J2000.9−1749	PKS 1958−179	0.65	45.9	2.30 ± 0.92	3.46 ± 0.98	6.7	J2001.0−1750
J2254.0+1613	3C 454.3	0.86	28.5	1.13 ± 0.66	6.26 ± 3.06	3.0	J2254.0+1608

Note. Columns are as follows: (1) 2FHL name; (2) other name; (3) redshift; (4) test statistic; (5) photon flux (50 GeV−2 TeV energy range, in units of 10^{-11} ph cm^{-2} s^{-1}); (6) spectral index (50 GeV−2 TeV energy range); (7) number of predicted photons; and (8) 3FGL association. All the information has been taken from Ackermann et al. (2016).

this indicates that their IC peak is typically located at relatively low (∼MeV) energies. Accordingly, FSRQs exhibit a soft γ-ray spectrum. In addition to that, absorption of γ-ray photons via pair production with the BLR radiation field can lead to an additional softening of the γ-ray spectrum of powerful FSRQs (e.g., Poutanen & Stern 2010), provided the γ-ray emission region is located inside the BLR. In most cases, the BLR (with a spherical geometry) can be considered as opaque for γ-rays with energies greater than $20\,\mathrm{GeV}/(1+z)$. The detection of VHE ($E > 50$ GeV) γ-rays from a few FSRQs (e.g., Aleksić et al. 2011) therefore, indicates that the γ-ray emitting region must be located close to or outside of the outer boundary of the BLR (e.g., Tavecchio et al. 2011). Overall, a detailed quantitative study of the γ-ray absorption by the BLR radiation field can provide clues about the location of the γ-ray emitting region in FSRQs.

In this work, we present a study of the time-averaged spectra of eight FSRQs that are included in the second catalog of hard *Fermi* Large Area Telescope (LAT) sources (2FHL; Ackermann et al. 2016) with the primary motivation to understand the radiation processes (leptonic or hadronic) dominating the high-energy emission of these objects. We derive the $\gamma\gamma$ opacity self-consistently with the location of the γ-ray emission region and predict the degree of X-ray and γ-ray polarization in both leptonic and hadronic emission scenarios. We also briefly discuss the role of these peculiar objects in probing the extragalactic background light (EBL, Hauser & Dwek 2001). Our aim is to study the overall time-averaged broadband behavior of these FSRQs rather than any of their specific activity states. In Section 2, we describe the sample. The details of the data reduction methodologies are given in Section 3. We outline the adopted leptonic and lepto-hadronic/hadronic emission models in Section 4 and briefly discuss the methods adopted to derive the central black hole mass and the accretion disk luminosity in Section 5. Results are presented and discussed in Section 6 and we conclude in Section 7. Throughout this paper, we assume a flat cosmology with $H_0 = 67.8\,\mathrm{km\,s^{-1}\,Mpc^{-1}}$ and $\Omega_{\mathrm{M}} = 0.308$ (Planck Collaboration et al. 2016).

2. Sample

The 2FHL is a catalog of sources detected in the 50 GeV–2 TeV energy range by the *Fermi*-LAT in its first 80 months of operation using the latest Pass 8 data set (Atwood et al. 2013). There are only 10 FSRQs present in the 2FHL. For comparison, the recently released 3FHL contains more than 150 FSRQs detected above 10 GeV (Ajello et al. 2017). This indicates a flux cutoff in the range of 10–50 GeV, possibly due to the steep γ-ray spectra of FSRQs. Moreover, EBL and possibly BLR absorption of the high energy γ-ray photons can also lead to the decreased number of significant γ-ray detections. Among the 10 FSRQs, 2FHL J0043.9+3424 ($z = 0.97$) does not have any existing multiwavelength observations, particularly X-rays, and 2FHL J0221.1+3556 is a gravitationally lensed quasar[7] ($z = 0.94$; e.g., Barnacka et al. 2016). Since there is no clear consensus about the lensing magnification factor, we do not consider this object as well as J0043.9+3424 and rather focus on the remaining eight sources with the well-characterized broadband SEDs. In Table 1, we present the basic 2FHL information on these FSRQs, and in Figure 1 the observed 2FHL spectra of all the sources are shown, along with their 3FGL and 1FHL γ-ray SEDs.

3. Data Compilation and Reduction

We use 2FHL γ-ray SEDs of all the objects as reported in three energy bands by Ackermann et al. (2016) and also consider their publicly available 1FHL (3 energy intervals) and 3FGL γ-ray spectra (5 bands; Ackermann et al. 2013, 2015). The γ-ray SEDs, from 0.1 GeV to 2 TeV, are corrected for EBL absorption following Domínguez et al. (2011). One can argue about the possible variability between these catalogs, since they cover different time periods. However, as noted before, our primary motivation is to study the average properties of these objects, hence considering time-averaged γ-ray SEDs is appropriate. Moreover, as can be seen in Figure 1, γ-ray spectra from the three catalogs join smoothly (except for J2000.9−1749), thus supporting our assumption.

We use all of the *Swift*-X-ray Telescope (XRT; Burrows et al. 2005) and UltraViolet and Optical Telescope (UVOT; Roming et al. 2005) observations covering the period of data collection for the 2FHL. In particular, the XRT data are analyzed using the online tool "*Swift*-XRT data product generator[8]" (Evans et al. 2009). This tool automatically corrects for pile-up, if any, and suitably selects source and background regions (see Evans et al. 2009 for details).

The downloaded source spectra are rebinned to have atleast 20 counts per bin and we perform the spectral fitting in XSPEC

[7] Recently, Falomo et al. (2017) found the redshift of the lensing galaxy doubtful.
[8] http://www.swift.ac.uk/user_objects/

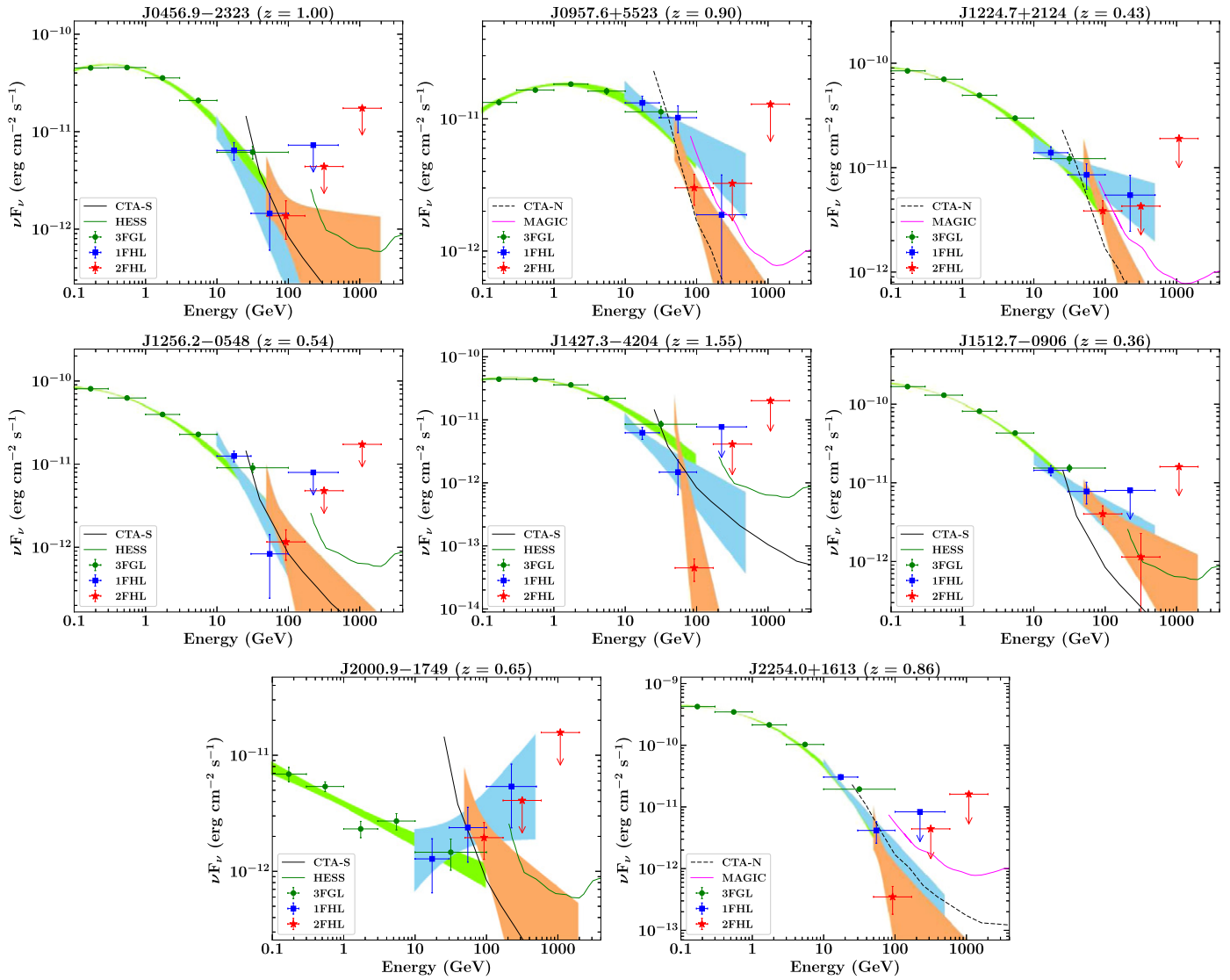

Figure 1. Gamma-ray SEDs of FSRQs studied in this work. Spectral data from the 3FGL, 1FHL, and 2FHL catalogs are represented by green circles, blue squares, and reds stars, respectively. Associated 1σ uncertainties are shown with shaded butterfly regions. We also show the sensitivity limits for 50 hr of integration with the MAGIC and HESS telescopes (pink and green solid lines; Holler et al. 2015; Aleksić et al. 2016), and the upcoming CTA-North (black dashed line) and CTA-South (black solid line). Note that we plot CTA-North and MAGIC sensitivities for northern hemisphere objects, whereas, for southern hemisphere sources, we show the sensitivity curves for CTA-South and HESS observatories.

(Arnaud 1996). We take the Galactic neutral hydrogen column density ($N_{\rm H}$) from Kalberla et al. (2005) and use two models, namely power-law and log-parabola, to perform the spectral fitting. The $N_{\rm H}$ value is kept frozen during the fitting. The best-fit model is determined by comparing the χ^2 values derived for the power-law (null hypothesis) and log-parabola models and computing the `f-test` probability.[9] We retain the log-parabola model if the null-hypothesis probability is $<10^{-4}$, thus indicating the presence of a significant ($>5\sigma$) curvature in the XRT spectrum. The results of the X-ray spectral analysis are provided in Table 2, where we also give the total number of XRT observations for each source.

Note that we have combined all of the XRT measurements taken during the period covered in the 2FHL catalog. Since blazars are known to exhibit large amplitude flux variations, one has to consider the possible impact it can have on the results also keeping in mind the fact the pointed mode operation of *Swift* compared to all-sky scanning mode operation of the *Fermi*-LAT. We have partially taken variability into account by excluding Windowed Timing (WT) mode XRT data. It is well known that the WT mode is used to observe a bright object (e.g., Mrk 421; Abdo et al. 2011) or when a source is in an elevated activity state (e.g., Kapanadze et al. 2017). By excluding the WT mode data, we have rejected very high flux states, such as 2010 November flare of J2254.0+1613 (3C 454.3). Moreover, in Section 6.3, we briefly discuss the possible implications of blazar variability to predict the high-energy polarization. In addition to that, since our primary objective is to study the overall average behavior of 2FHL FSRQs, rather than any of their specific activity states, we believe that the results derived under this assumption are robust.

UVOT snapshots are first summed using the tool `uvotimsum` and then source magnitudes are extracted from a circular region

[9] https://heasarc.gsfc.nasa.gov/xanadu/xspec/manual/node83.html

Table 2
Summary of the X-Ray Analysis

Name	#	Exp. (ks)	N_H (10^{20} cm^{-2})	Γ_X	β_X	F_X (10^{-12} erg cm^{-2} s^{-1})	Stat. χ^2/dof
J0456.9−2323	16	54.1	2.84	$1.55^{+0.06}_{-0.07}$		$1.24^{+0.07}_{-0.07}$	48.42/58
J0957.6+5523	8	27.3	0.93	$1.72^{+0.12}_{-0.11}$	...	$0.70^{+0.08}_{-0.08}$	24.01/18
J1224.7+2124	97	182.6	2.01	$1.85^{+0.02}_{-0.02}$	$-0.48^{+0.04}_{-0.05}$	$5.93^{+0.08}_{-0.12}$	397.06/399
J1256.2−0547	244	422.3	2.05	$1.49^{+0.01}_{-0.01}$	$0.15^{+0.02}_{-0.02}$	$15.40^{+0.10}_{-0.10}$	772.77/675
J1427.3−4204	53	182.4	7.63	$1.15^{+0.04}_{-0.04}$	$0.51^{+0.07}_{-0.06}$	$3.49^{+0.09}_{-0.09}$	376.83/345
J1512.7−0906	168	318.6	6.89	$1.38^{+0.02}_{-0.02}$	$-0.07^{+0.03}_{-0.03}$	$11.00^{+0.11}_{-0.15}$	656.58/638
J2000.9−1749	3	9.4	6.93	$1.65^{+0.18}_{-0.18}$	...	$1.67^{+0.24}_{-0.19}$	8.26/11
J2254.0+1613	153	303.4	6.63	$1.21^{+0.01}_{-0.01}$	$0.31^{+0.02}_{-0.02}$	$42.65^{+0.30}_{-0.30}$	968.02/731

Note. Second column represents the total number of XRT observations for each source. The spectral parameter Γ_X represents the best-fit photon index for a power-law model or slope at the pivot energy (fixed to 1 keV) for the log-parabola model. On the other hand, β_X is the curvature term for the log-parabola model. F_X is the integrated X-ray flux in the energy range of 0.3–10 keV.

of 5″ centered at the target quasar, using the task `uvotsource`. The background is estimated from a nearby circular region of 30″ free from source contamination. We correct source magnitudes for Galactic extinction following Schlafly & Finkbeiner (2011) and convert to flux units using the calibrations of Breeveld et al. (2011).

4. Radiative Models

The basic assumption, when averaging years of the multi-frequency data, is that the emitting region is considered to be a quasi-stationary acceleration zone, where a continuous flow of particles (leptons or hadrons) are injected and then radiate, moving along with a certain bulk Lorentz factor Γ (e.g., Hervet et al. 2016). This is because a single emitting region moves along the jet at relativistic speed; in several years, it moves by several light-years, expanding accordingly (and seeing varying external photon fields), while we keep the location of the emitting region fixed. Therefore, the SED parameters derived from such an averaged analysis provide information about the overall average behavior of the blazar rather than its specific activity state.

4.1. Leptonic Emission Model

We use a simple one-zone leptonic emission model to describe the broadband SEDs of 2FHL FSRQs, following Ghisellini & Tavecchio (2009). In particular, we assume a spherical emission region (or blob) located at a distance $R_{\rm diss}$ from the central black hole of mass $M_{\rm BH}$. The blob is filled with highly energetic electrons. Here, we do not consider a self-consistent cooling model. Instead, we assume that the electron population follows a smooth broken power-law distribution of the following form:

$$N(\gamma) = N_0 \frac{(\gamma_{\rm b})^{-s1}}{(\gamma/\gamma_{\rm b})^{s1} + (\gamma/\gamma_{\rm b})^{s2}}, \quad (1)$$

where N_0 is the normalization constant (cm^{-3}) and $s1$, $s2$ are the spectral indices below and above the break energy $\gamma_{\rm b}$, respectively. We consider both SSC and EC for the high-energy emission. The accretion disk is considered to be Shakura & Sunyaev (1973) type and its spectrum is given by a multitemperature annular blackbody with a temperature distribution (Frank et al. 2002)

$$T = \left[\frac{3R_{\rm S}\, L_{\rm disk}}{16\pi\, \eta_{\rm acc}\, \sigma_{\rm SB}\, R^3}\left\{1 - \left(\frac{3R_{\rm S}}{R}\right)^{1/2}\right\}\right]^{1/4}, \quad (2)$$

where $L_{\rm disk}$ is the disk luminosity, $R_{\rm S}$ is the Schwarzschild radius, $\sigma_{\rm SB}$ is the Stefan–Boltzmann constant, and $\eta_{\rm acc}$ is the accretion efficiency taken as 10%. The BLR and the dusty torus are assumed to reprocess a fraction (10% and 30%, respectively) of $L_{\rm disk}$. Their spectral profiles are characterized by a spherical blackbody located at a distance $R_{\rm BLR} = 10^{17}\, L_{\rm disk,45}^{1/2}$ cm and $R_{\rm torus} = 2.5 \times 10^{18} L_{\rm disk,45}^{1/2}$ cm, respectively, where $L_{\rm disk,45}$ is the accretion disk luminosity in units of 10^{45} erg s^{-1}. We also consider the presence of the X-ray emitting corona recycling 30% of $L_{\rm disk}$ and its spectral shape is assumed to be a flat power law with an exponential cutoff. In the comoving frame, the radiative energy densities of these external AGN components are calculated as a function of $R_{\rm diss}$ (Ghisellini & Tavecchio 2009). We calculate the powers that the jet carries in the form of electrons ($P_{\rm e}$), magnetic field ($P_{\rm m}$), and cold protons ($P_{\rm p}$). In particular, the kinetic jet power, is derived by assuming equal number densities of emitting electrons and cold protons (e.g., Celotti & Ghisellini 2008).

4.2. Lepto-hadronic Emission Model

We use the code of Böttcher et al. (2013) for the one-zone hadronic model. Unlike the leptonic model, our hadronic model involves a semi-analytical evolution of particle injection, cooling, and escape, to a quasi-equilibrium state by solving steady-state Fokker–Planck equations. For the electrons and positron pairs, our model includes synchrotron cooling, which is the dominating energy loss process in the strong magnetic field required for these models and energy-independent electron escape. We also consider injection terms representing primary electron injection, pion/muon decay, and $\gamma\gamma$ pair production. Here, electron SSC can be important in the high-energy SED component, but in general the SSC cooling rate is much lower than that of the synchrotron process. For the protons, since the radiative cooling timescale is much longer than that of the electrons, we also include adiabatic and photon-pion production losses. In this way, particle cooling is self-consistently evaluated. The quasi-equilibrium proton distribution is then derived based on the energy loss terms, primary

proton injection, and energy-independent proton escape. Our choice of parameters are generally consistent with physical conditions of small muon and pion contributions described in Böttcher et al. (2013), thus we ignore their contributions to the spectrum. We choose the primary proton injection spectra as straight power-law distributions with a turnover at the high energy $\gamma_{b,p}$,

$$Q_p(\gamma) = Q_{0,p}(\gamma/\gamma_{b,p})^{s_{1,p}}, \quad 1 \leqslant \gamma < \gamma_{b,p}$$
$$= Q_{0,p}(\gamma/\gamma_{b,p})^{s_{2,p}}, \quad \gamma_{b,p} \leqslant \gamma < \gamma_{2,p}, \tag{3}$$

where $s_{1,p}$ is the power-law index and $s_{2,p}$ is the power-law index of the high-energy turnover. This turnover is a natural result of the Fermi acceleration based on numerical simulations (Sironi & Spitkovsky 2011; Guo et al. 2016), which can be approximated by a short power law that covers less than one decade of particle Lorentz factor. For the primary electron spectra, because of the very strong cooling, we expect that the high-energy electrons are sufficiently cooled, thus the high-energy turnover is not observable. Therefore, we choose straight power-law spectra,

$$Q_e(\gamma) = Q_{0,e}\gamma^{s_e}, \ \gamma_{1,e} \leqslant \gamma < \gamma_{2,e} \tag{4}$$

where $\gamma_{1,e}$ is the low-energy cutoff of the electron spectra, which corresponds to a background thermal temperature, $\gamma_{2,e}$ is the high-energy cutoff, and s_e is the electron spectral index.

4.3. High-energy Polarization Model

We predict the high-energy (X-ray and γ-ray) polarization degree for both the leptonic and hadronic models following Zhang & Böttcher (2013). Their calculations considered a perfectly ordered magnetic field, thus representing upper limits to the expected degree of polarization. Therefore, a generalization with the correction for a partially ordered magnetic field is necessary, as described below.

The general formalism for the observed high-energy polarization degree is

$$\Pi(\nu) = Z_{\rm m}\frac{P_{\rm pol}(\nu)}{P_{\rm tot}(\nu)}, \tag{5}$$

where $Z_{\rm m}$ is a correction factor due to the partially ordered magnetic field, and $P_{\rm pol}$, $P_{\rm tot}$ are the polarized and total radiation power in a perfectly ordered magnetic field. Given that the low-energy synchrotron component and high-energy SED component are cospatial for both leptonic and hadronic models, the optical polarization degree and high-energy polarization degree should be corrected by the same factor for a partially ordered magnetic field. The same assumption has been used in Bonometto & Saggion (1973) and Zhang & Böttcher (2013). More recently, this conjecture of equal depolarization factors has been confirmed for a 3D multizone hadronic model developed by Zhang et al. (2016), where the magnetic field is partially ordered.

To evaluate the correction factor $Z_{\rm m}$, we first collect the average optical polarization degree ($\Pi_{\rm o}$) for each source (see Table 5). We collect this information from Steward and RoboPol observatories (Smith et al. 2009; Pavlidou et al. 2014). The theoretical upper limit for the optical polarization degree is around 70%–75% for an electron power-law distribution of index 2–3 (Rybicki & Lightman 1985). Given that the average optical polarization degrees are not obtained simultaneously with our *Fermi* observations, here we choose a conservative value at 70%. Clearly the average observed optical polarization degree $\Pi_{\rm o}$ is lower than the theoretical value of 70%. This is mainly because of two depolarization effects, namely the partially ordered magnetic field and unpolarized thermal contributions to the optical emission. The correction introduced by the partially ordered magnetic field is $Z_{\rm m}$, while the correction by the unpolarized thermal contribution is $P_{\rm syn}/(P_{\rm syn}+P_{\rm th})$, where $P_{\rm syn}$ and $P_{\rm th}$ are the synchrotron and thermal radiation power derived from spectral fitting. Therefore, we have

$$\Pi_{\rm o} = Z_{\rm m}\frac{P_{\rm syn}}{P_{\rm syn}+P_{\rm th}} \times 70\%. \tag{6}$$

Given $\Pi_{\rm o}$ for each source and the fact that leptonic and hadronic models predict a very similar low-energy SED component, so that the ratio between the primary electron synchrotron and thermal emission are identical for both models, $Z_{\rm m}$ is then identical for the two models. We list the resulting values of $Z_{\rm m}$ in Table 5.

For the leptonic model, the high-energy emission is a combination of SSC ($P_{\rm SSC}$) and EC ($P_{\rm EC}$). EC radiation is essentially unpolarized. Therefore, the frequency-dependent polarization degree is predicted to be

$$\Pi_{\rm lep}(\nu) = Z_{\rm m}\frac{P_{\rm SSC,pol}(\nu)}{P_{\rm SSC,tot}(\nu)+P_{\rm EC,tot}(\nu)}, \tag{7}$$

where $P_{\rm SSC,pol}(\nu)$ is the polarized SSC power in a perfectly ordered magnetic field, evaluated following Bonometto & Saggion (1973) and Zhang & Böttcher (2013), and $P_{\rm SSC,tot}(\nu)$ and $P_{\rm EC,tot}(\nu)$ are the SSC and EC powers derived from the modeling. On the other hand, the X-ray and γ-ray emission in the hadronic model are from proton synchrotron ($P_{\rm p}$), pair synchrotron ($P_{\rm pair}$), and an SSC contribution from the primary electrons ($P_{\rm SSC}$). Similarly, the polarization degree is

$$\Pi_{\rm had}(\nu) = Z_{\rm m}\frac{P_{\rm p,pol}(\nu)+P_{\rm pair,pol}(\nu)+P_{\rm SSC,pol}(\nu)}{P_{\rm p,tot}(\nu)+P_{\rm pair,tot}(\nu)+P_{\rm SSC,tot}(\nu)}. \tag{8}$$

5. Black Hole Mass and the Accretion Disk Luminosity

The black hole mass, $M_{\rm BH}$, and accretion disk luminosity, $L_{\rm disk}$, are the two crucial ingredients to model the accretion disk contribution to the SED of an FSRQ. With the knowledge of the disk luminosity, the external photon fields can be fully parameterized in terms of distance of the emission region from the central engine (Ghisellini & Tavecchio 2009). This is also crucial to determine the $\gamma\gamma$ pair production optical depth as a function of the dissipation distance which depends on the energy density of the interacting radiation fields (e.g., Böttcher & Els 2016, and references therein).

Two widely accepted methods to calculate $M_{\rm BH}$ and $L_{\rm disk}$ are (a) to use single-epoch optical spectroscopy with the assumption that the BLR is virialized (e.g., Shaw et al. 2012) and (b) the modeling of the optical–UV SED with a Shakura & Sunyaev (1973) disk if this part of the SED is accretion disk dominated. It has been found in recent studies that both the methods reasonably agree (see, e.g., Paliya et al. 2017).

We have collected the optical spectroscopic emission line parameters from the literature to derive both $M_{\rm BH}$ and $L_{\rm disk}$. We take the Mg II line luminosity of J0456.9−2323 and

J1427.3−4204 from Stickel & Kuehr (1993) and Stickel et al. (1989) respectively. By following the empirical relation and line coefficients of Shaw et al. (2012), we derive both $L_{\rm disk}$ and $M_{\rm BH}$. In particular, $L_{\rm disk}$ is computed following the scaling relations of Francis et al. (1991) and Celotti et al. (1997) and assuming that the BLR reprocesses 10% of $L_{\rm disk}$. Shaw et al. (2012) reported $M_{\rm BH}$ and Mg II line luminosity for J0957.6+5523 and J1224.7+2124, which we use to calculate $L_{\rm disk}$. For J1256.2−0548, J1512.7−0906, and J2254.0+1613, we take their $M_{\rm BH}$ and $L_{\rm disk}$ from the literature (Pian et al. 1999; Woo & Urry 2002; Dai et al. 2007; Bonnoli et al. 2011; Paliya et al. 2015). For J2000.9−1749, Mg II line information are available in Oke et al. (1984), which we use to derive $M_{\rm BH}$ and $L_{\rm disk}$.

6. Results and Discussion

We generate steady-state, i.e., time-averaged, broadband SEDs of all eight FSRQs following the details outlined in Section 3 and reproduce them using both leptonic and lepto-hadronic emission scenarios. The leptonic model SEDs are presented in Figure 2 and the associated SED parameters are given in Table 3. The results of the lepto-hadronic SED modeling are shown in Figure 3 and we provide the physical parameters derived from the modeling in Table 4. Using the results of the SED modeling, we compute the degree of X-ray and γ-ray polarization predicted by the leptonic and hadronic models. The results are shown in Figure 4. Table 5 provides our prediction about the degree of polarization that would be detected from sources under study at 1 keV and at 1 MeV energies, correcting for partially ordered magnetic field as described in Section 4.3.

6.1. Leptonic Modeling

Our SED modeling procedure does not involve any statistical fitting method and hence there could be possible degeneracy in the SED parameters. However, depending on the quality of the observations, the SED parameters are reasonably constrained. Before the modeling, we fix to the following parameters either due to a priori knowledge or based on physical considerations: $M_{\rm BH}$ and $L_{\rm disk}$ (Section 5), $\gamma_{\rm min}$, $\theta_{\rm view}$ and the fraction of $L_{\rm disk}$ reprocessed by the BLR, torus, and the X-ray corona (e.g., Jorstad et al. 2005; Ghisellini & Tavecchio 2009; Lister et al. 2013). This fixes the radiative energy densities used for the EC calculation. Among eight free parameters: N_0, $s1$, $s2$, B, $R_{\rm diss}$, Γ, $\gamma_{\rm b}$, and $\gamma_{\rm max}$, the slopes of the electron energy distribution, $s1$ and $s2$, can be constrained from the shapes of the X-ray and γ-ray SEDs (see also, Paliya et al. 2017). Whenever the optical spectrum is found to be synchrotron dominated, it provides further constrains to the high-energy slope $s2$. We determine the size of the emission region by assuming it to cover the entire jet cross-section whose semi-opening angle is assumed to be 0.1 rad. The Compton dominance, which is the ratio of the high-to-low-energy humps, enables us to determine the ratio of the radiation to magnetic energy density, $U_{\rm rad}/U_{\rm mag}$, and hence constrains the location of the emission region. This is because, in our model, these quantities are a function of $R_{\rm diss}$. Furthermore, for a major fraction of sources, we find the optical–UV emission to be synchrotron dominated, which suggests a high level of SSC. Once the synchrotron spectrum is determined from the optical–UV SED, a high level of SSC emission demands a relatively low magnetic field B. This is because, with smaller B, higher number of electrons are needed to achieve the same synchrotron flux level. As the electrons number density goes up, so does the SSC flux level. Similarly, both SSC and EC fluxes (constrained from the observed X-ray and γ-ray SEDs) also provide a tight constraint to Γ. An increase in Γ (or equivalently Doppler factor δ) decreases the electron number density since fewer electrons are needed to maintain a given synchrotron flux level, thus decreasing both SSC and EC. However, overall EC flux increases since the enhancement in δ also leads to an increase in the comoving frame external photon densities (Dermer 1995).

The leptonic modeling reasonably reproduces most of the observed SEDs of 2FHL FSRQs. The accretion disk emission is observed at optical–UV frequencies in J1224.7+2124, J1427.3−4204, and J1512.7−0906. On the other hand, the optical–UV emission in the remaining five sources is dominated by the synchrotron radiation. The high-energy spectra of these objects can be reproduced by a combination of SSC and EC processes. In our model, the radiative energy densities are a function of the dissipation distance from the central black hole. Our modeling parameters suggest that the emission region is outside of the inner boundary of the BLR (Table 3). This is evident from the fact that all of the sources are detected above 50 GeV, which requires the effect of γ-ray absorption by BLR photons to be negligible. However, the emission region is likely close to the BLR, because all the objects have a Compton dominance significantly larger than unity, implying that the external photon energy density dominates over the magnetic energy density. In Figure 5, we present the variation of the comoving frame radiative energy densities with distance from the central black hole and also show the location of the emission region as inferred from the modeling. We can see that both BLR and torus energy densities contribute to the observed γ-ray emission, but the dominant fraction comes from the BLR (see also Joshi et al. 2014 for similar arguments). The EC peak frequency ($\nu^{\rm IC}_{\rm peak}$) is a further diagnostic of the primary γ-ray emission mechanism. In the Thomson regime, the peak of the IC component is

$$\nu^{\rm EC}_{\rm peak} \simeq \frac{\nu_{\rm seed}\Gamma^2\gamma_{\rm b}^2}{(1+z)}, \quad (9)$$

where $\nu_{\rm seed}$ is the characteristic frequency of seed photons for the EC mechanism ($\sim 10^{15}$ Hz or $\sim 10^{13}$ Hz for BLR and torus photons, respectively). The derived $\gamma_{\rm b}$ has a rather low value and therefore higher energy seed photons can explain the observed IC peak located around MeV−GeV energies, which is consistent with BLR photons as the seed photons for IC. Moreover, above 50 GeV or so, interaction of BLR photons with jet electrons occurs at Klein–Nishina energies, whereas, IC scattering of torus photons still remains within the Thomson regime (e.g., Cerruti et al. 2013; Dermer et al. 2014). To summarize, the emission region is probably located at the outer edge of the BLR.

A Compton dominated SED, as observed for all of the sources, indicates a considerably smaller magnetic jet power compared to the kinetic luminosity. This, in turn, hints at a low magnetization of the emission region (e.g., Janiak et al. 2015). Furthermore, a comparison of the kinetic jet power with the accretion disk luminosity (Table 3) suggests that the jet power exceeds the accretion luminosity, which is now a well-known

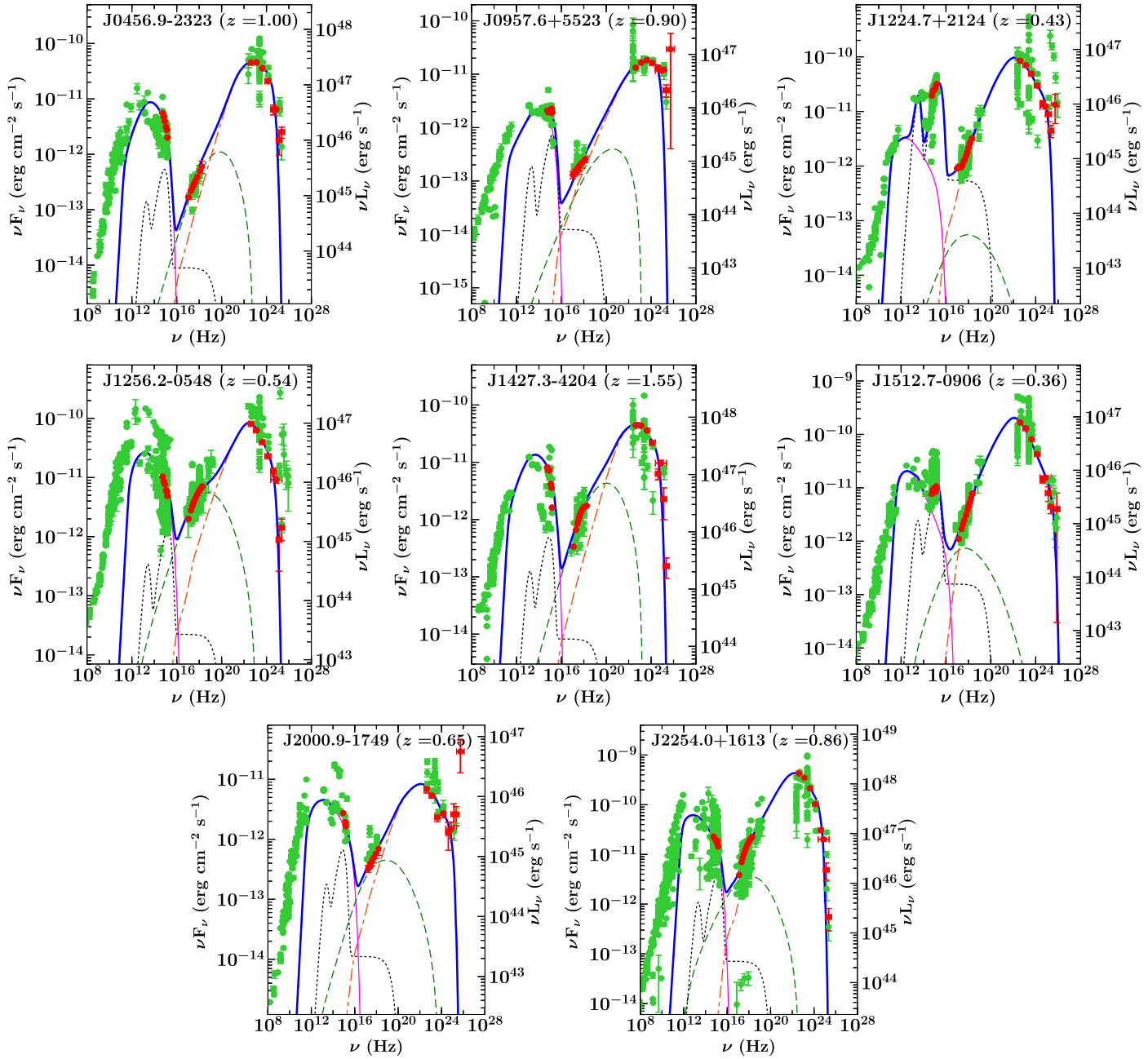

Figure 2. Leptonic modeling of the broadband SEDs of 2FHL FSRQs studied here. The data used for the modeling is shown with red filled circles, whereas, green circles represent the archival information. Pink thin solid, green dashed, and orange dashed–dashed–dotted lines correspond to the synchrotron, SSC, and EC mechanisms, respectively. The thermal emissions from the dusty torus, the accretion disk, and the X-ray corona are shown with the black dotted line. The overall radiative output is represented by the blue thick solid line. Note that the *Fermi*-LAT data points are corrected for EBL absorption following Domínguez et al. (2011).

fact (Ghisellini et al. 2014). However, note that the jet power computation is a strong function of assumed number of protons per electron. If a few pairs are present in the emission region, thus reducing the number density of protons, the budget of the jet power will decrease (see, e.g., Madejski et al. 2016; Pjanka et al. 2017). Moreover, Sikora et al. (2016) proposed a spine-sheath structured jet that predicts a lower jet power with respect to that computed by assuming a uniform single-zone emission.

6.2. Hadronic Modeling

The hadronic model produces similarly good fits compared to the leptonic model. In particular, it predicts higher flux beyond 50 GeV than the leptonic model. Here, we fix the viewing angle and the Lorentz factors the same as the leptonic fits to reduce the number of free parameters. The self-consistent treatment of cooling effects employed in the hadronic fits promises less degeneracy in the model parameters than the leptonic fits. The cascading secondaries typically have softer spectra than the primary protons (Böttcher et al. 2013). Given the very hard spectra from X-ray to γ-ray, all sources require a dominating proton synchrotron contribution for the high-energy spectral component. Therefore, the underlying proton spectrum is well constrained by the observed X-ray to γ-ray SED, which suggests a single power-law shape with a softer turnover near the high energy end. This turnover, however, is not consistent with the

Table 3
List of the Parameters Used/Derived in the Leptonic SED Modeling of 2FHL FSRQs

2FHL Name [1]	θ_v [2]	M_{BH} [3]	L_{disk} [4]	$s1$ [5]	$s2$ [6]	B [7]	U_e [8]	Γ [9]	γ_b [10]	γ_{max} [11]	R_{diss} [12]	R_{BLR} [13]	R_{blob} [14]	P_m [15]	P_e [16]	P_p [17]
J0456.9−2323	2	9.0	45.6	1.6	3.9	0.8	0.01	18	833	5000	0.10	0.06	0.010	44.8	44.6	46.5
J0957.6+5523	3	8.4	45.6	2.0	3.4	0.6	0.02	14	1762	7000	0.10	0.06	0.010	44.4	44.6	47.0
J1224.7+2124	3	8.8	46.5	1.8	3.7	0.5	0.01	13	226	8000	0.24	0.18	0.024	44.9	44.4	46.8
J1256.2−0548	3	8.5	45.3	1.8	3.9	1.7	0.10	14	352	5000	0.06	0.05	0.006	44.9	44.8	47.1
J1427.3−4204	3	9.0	46.0	1.6	3.7	0.8	0.02	15	852	7000	0.16	0.10	0.016	45.1	45.0	46.9
J1512.7−0906	3	8.8	45.7	1.9	4.0	1.2	0.02	18	206	10000	0.10	0.08	0.010	45.2	44.8	46.8
J2000.9−1749	3	9.0	45.2	1.8	3.6	1.3	0.05	16	272	8000	0.06	0.04	0.006	44.7	44.6	46.9
J2254.0+1613	3	9.0	46.3	2.1	3.8	3.0	0.03	18	215	3500	0.16	0.14	0.016	46.4	45.4	48.0

Note. Columns are as follows: (1) 2FHL name; (2) viewing angle, in degrees; (3) central black hole mass, in log scale; (4) accretion disk luminosity (erg s^{-1}), in log scale; (5) and (6) broken power-law spectral indices; (7) magnetic field, in Gauss; (8) particle energy density, in erg cm^{-3}; (9) bulk Lorentz factor; (10) break Lorentz factor; (11) Maximum Lorentz factor; (12) distance of the emission region from the black hole, in parsecs; (13) size of the BLR, in parsecs; (14) size of the emission region, in parsecs; (15), (16), and (17) jet powers in magnetic field, electrons, and protons, respectively. The characteristic temperature of the dusty torus is taken as 500 K and we assume γ_{min} as unity, for all the sources.

cooling break that is self-consistently treated in the hadronic code. Instead, we suggest that it is due to the particle acceleration. In practice, shock and magnetic reconnection can produce a power-law shaped spectrum with a turnover at the high energy end. Numerical simulations have shown that this turnover is not an exponential cutoff, but rather like a softer power law that extends to about one decade in the particle Lorentz factor (e.g., Sironi & Spitkovsky 2011; Guo et al. 2016). Our proton spectral parameters are generally consistent with the numerical particle acceleration simulations. Therefore, if the γ-ray of these hard spectrum *Fermi* sources is produced through proton synchrotron, then the highest protons should not be efficiently cooled within one light crossing time. Based on our fitting, this suggests an upper limit on the magnetic field $B \lesssim 100$ G.

It is clear that the emission beyond ∼50 GeV is not perfectly consistent with an exponential cutoff. We suggest that this feature is due to the synchrotron of cascading pairs. We notice that this contribution is generally small compared to the proton synchrotron. Since the cascading pair flux is proportional to the low-energy photon density, then the low-energy photon density should be small. Therefore, the emission region is likely beyond the BLR, so that the low-energy photons are from the primary electron synchrotron. Given the observed luminosity, the low photon density indicates a large emission blob. Our fitting results suggest that the size is on the order of $\sim 10^{15}$ cm.

We find that the X-ray spectra are well fit by the synchrotron of primary protons and cascading pairs. Therefore, the SSC from the primary electrons must be very low. Then the ratio between the optical emission, which is dominated by the synchrotron of the primary electrons, and the X-ray emission, which is the upper limit of the primary electron SSC, gives a lower limit on the magnetic field strength. Our fitting suggests a lower limit on the order of ∼10 G. This magnetic field range suggests that the low-energy spectral component must originate from the synchrotron of primary electrons. Thus the underlying electron spectral shape can be constrained by the observed optical spectra.

Our fitting results generally suggest that the jet energy composition is $P_e < P_m \lesssim P_p$. Our results are generally consistent with previous hadronic model fits (see, e.g., Böttcher et al. 2013). In the hadronic model, the proton power P_p is generally larger than the accretion luminosity, which often requires a super Eddington accretion (Zdziarski & Böttcher 2015). We notice that, although all the model's parameters are constrained by the multiwavelength spectra, the parameter space is rather large. For example, the magnetic field strength can range from ∼10 to ∼100 G. To further constrain the model parameters, additional observational constraints, such as the time-dependent signatures, are necessary. Zhang et al. (2016) has demonstrated that the time-dependent multiwavelength light curves and polarization signatures can stringently constrain the hadronic model parameters. However, a detailed time-dependent, variability focused study is beyond the scope of this paper.

6.3. X-Ray Polarization and Anticipation for Future X-Ray Polarimetric Satellites

It is obvious that the high-energy polarization signatures are drastically different between the leptonic and hadronic models. Since all eight sources are FSRQs, they exhibit strong thermal components, which lead to high EC contribution in the high-energy component. Generally speaking, EC can be considered unpolarized. Moreover, SSC reduces the seed synchrotron polarization, thus its polarization degree is mostly $\lesssim$40%. As we can see in Figure 4, the maximal leptonic polarization degree is only 20%–40% at X-rays, where SSC generally dominates, and then quickly drops to zero toward higher energies, where EC becomes dominant. On the other hand, the synchrotron emission of protons and cascading pairs dominates the high-energy emission in the hadronic model. Here the polarization degree is 70%–80%. This makes the maximal hadronic polarization degree much higher than that of the leptonic model.

An interesting feature of the hadronic modeling is that all these hard spectrum FSRQs have a straight and dominating proton synchrotron SED component. The SSC of primary electrons and the synchrotron of cascading pairs only mildly lower the polarization degree at X-rays. Therefore, the X-ray and γ-ray polarization of the FSRQs are nearly identical. For the leptonic model, however, the X-ray polarization is clearly higher than the γ-ray polarization. This feature can be examined by future X-ray and γ-ray polarimeters as a further diagnostic of the two models for FSRQs.

To give a better prediction of what we expect from future high-energy polarimetry, we estimate the corrected high-energy polarization degree at 1 keV and 1 MeV. The depolarization factor due to partially ordered magnetic field is taken into account, as detailed in Section 4.3. We use both the average and high activity state polarization degrees, obtained by Steward Observatory and RoboPol (Smith et al. 2009; Pavlidou et al. 2014), to

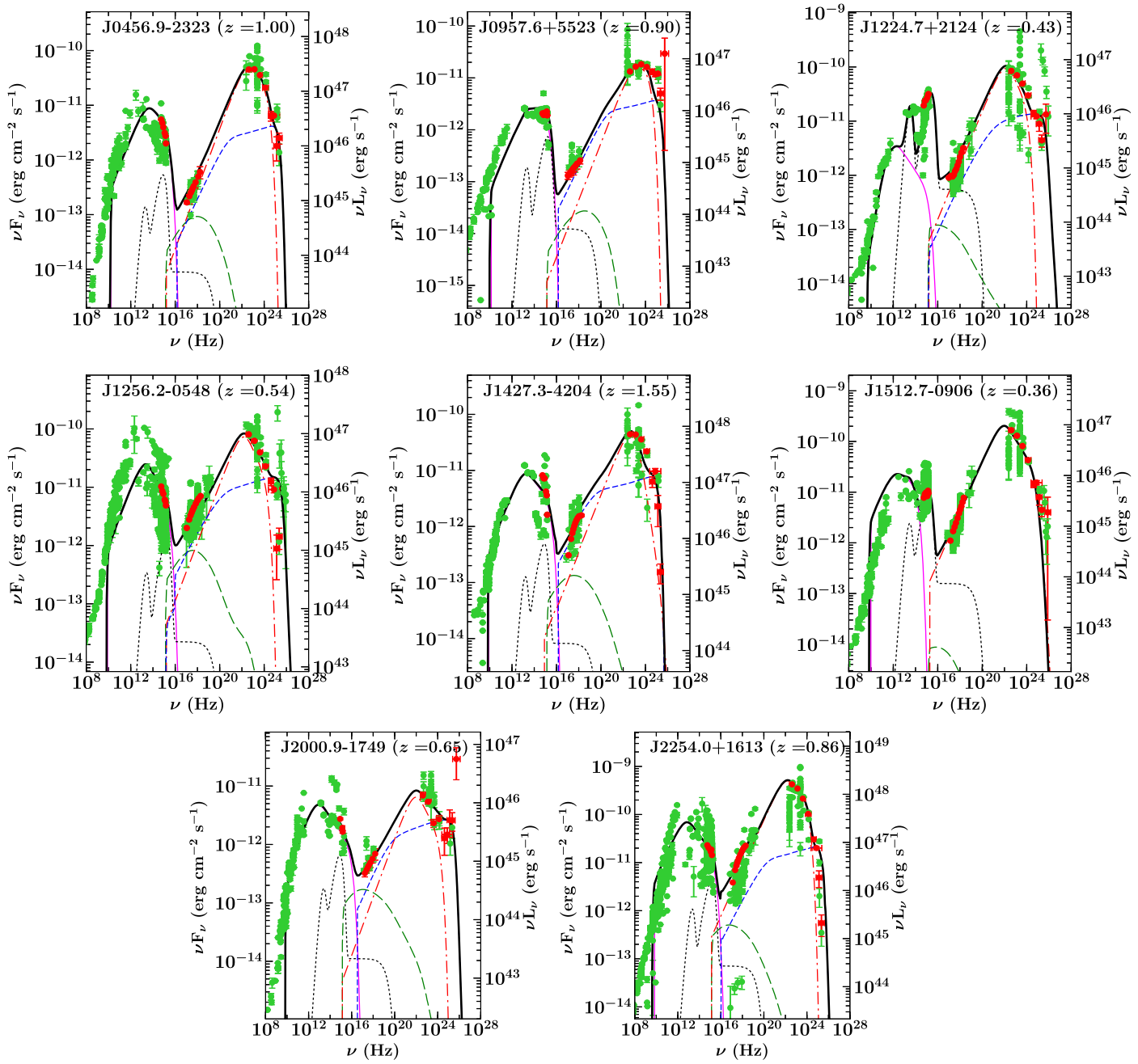

Figure 3. Broadband SEDs of 2FHL FSRQs modeled with the lepto-hadronic radiative model. Electron synchrotron and SSC models are shown with solid thin pink and green long dashed lines, respectively. On the other hand, proton synchrotron and SSC emissions are represented by red dashed–dotted and blue small dashed lines, respectively. Black thick solid line corresponds to the sum of all the radiative components. Other information is the same as in Figure 2.

estimate the potential range of high-energy polarization degree. The results are listed in Table 5. During the average state, the optical polarization degree is relatively low, ∼10%. We estimate that the corrected leptonic polarization degree is ∼5%, and the hadronic is ≳10% at 1 keV. Since the flux level and the polarization degree are rather low during the average state, it is hard for next generation polarimeters to detect high-energy polarization signatures. In addition, it is well known that the optical polarization signatures are highly variable, which indicates changes in the magnetic field (Marscher 2014; Zhang et al. 2015). The same can happen to the high-energy polarization, so that the averaged polarization degree may be even lower than what we estimate here. Therefore, we argue that the X-ray and γ-ray polarization signatures may not be detectable for either leptonic or hadronic models by averaging a long period of high-energy polarization monitoring.

On the other hand, during the elevated activity state, not only can the flux be higher, but the optical polarization degree can also be higher, ∼30%. Here we find that the X-ray/γ-ray polarization in the leptonic scenario is ∼15%, while the hadronic polarization is ≳30%. Zhang et al. (2016) have shown that the hadronic high-energy polarization signatures are similar between the quiescent state and the active state, and we expect the same for the leptonic model. Therefore, we recommend that the next generation polarimeters should focus on the active state for best high-energy polarization detection.

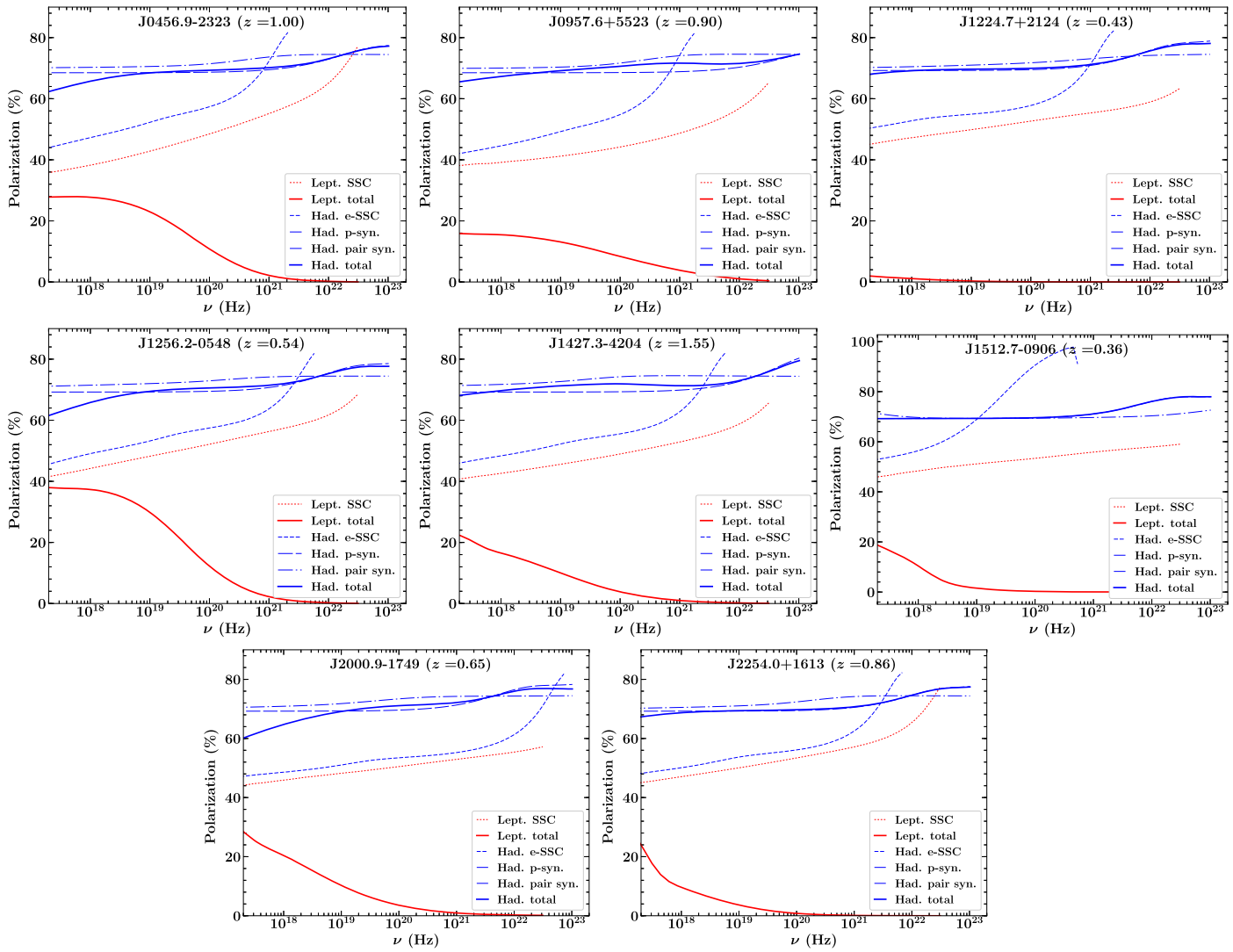

Figure 4. Degree of X-ray polarization computed by considering both leptonic and hadronic emission scenarios. The components are appropriately labeled. See the text for details.

Table 4
List of the Parameters Used/Derived in the Hadronic SED Modeling of 2FHL FSRQs

2FHL Name [1]	θ_v [2]	B [3]	Γ [4]	s_e [5]	$\gamma_{1,e}$ [6]	$\gamma_{2,e}$ [7]	$s_{1,p}$ [8]	$s_{2,p}$ [9]	$\gamma_{b,p}$ [10]	$\gamma_{2,p}$ [11]	R_{blob} [12]	P_m [13]	P_e [14]	P_p [15]
J0456.9−2323	2	100	18	2.5	80	700	1.9	3.5	10^8	8×10^8	3.2×10^{-4}	46.1	43.2	47.9
J0957.6+5523	3	100	14	2.0	80	700	1.9	3.0	2×10^8	10^9	3.2×10^{-4}	45.9	42.8	47.3
J1224.7+2124	3	30	13	2.6	30	900	2.0	3.8	1.2×10^8	10^9	2.3×10^{-4}	44.4	43.3	49.0
J1256.2−0548	3	50	14	2.8	90	1000	2.0	3.8	10^8	10^9	4.8×10^{-4}	45.6	43.6	48.5
J1427.3−4204	3	100	11	2.5	70	1000	2.0	2.4	4×10^8	5×10^9	1.3×10^{-3}	46.9	43.5	48.3
J1512.7−0906	3	50	18	2.2	20	200	2.0	3.7	7×10^7	5×10^9	2.6×10^{-3}	47.3	43.0	48.0
J2000.9−1749	3	50	14	2.5	50	2000	2.0	3.7	8×10^7	10^9	2.9×10^{-4}	45.2	43.5	48.0
J2254.0+1613	3	50	18	2.6	50	1000	2.0	3.5	10^8	10^9	3.2×10^{-3}	47.5	44.2	49.2

Note. Columns are as follows: (1) 2FHL name; (2) viewing angle, in degrees; (3) magnetic field, in Gauss; (4) Bulk Lorentz factor; (5) power-law spectral indices for primary electrons; (6) and (7) minimal and maximal Lorentz factors for primary electrons; (8) and (9) power-law spectral indices for primary protons before and after the spectral break; (10) and (11) spectral break and maximal Lorentz factors for primary protons; (12) size of the emission region, in parsecs; (13), (14), and (15) jet powers in magnetic field, electrons, and protons, respectively. We assume $\gamma_{1,p}$ as unity for all the sources.

We notice that the hadronic polarization degree is consistently higher (or comparable) than the optical counterpart. This is easy to understand, because the optical polarization is generally contaminated by an unpolarized thermal component in FSRQs, while the X-ray and γ-ray polarization is mostly due to synchrotron.

Table 5
High Energy Polarization at 1 keV and 1 MeV Derived for 2FHL FSRQs

2FHL Name	Optical Pol. (%)	Z_m	lep. Pol. (1 keV, %)	had. Pol. (1 keV, %)	lep. Pol. (1 MeV, %)	had. Pol. (1 MeV, %)
(1)	(2)	(3)	(4)	(5)	(6)	(7)
		Average Activity State				
J0456.9−2323	9.9*	0.16	4.2	9.5	1.0	10.1
J0957.6+5523	5.7†	0.10	1.6	6.6	1.0	7.2
J1224.7+2124	5.4*	0.99	1.8	50.8	0.0	55.3
J1256.2−0548	15.0*	0.23	8.7	14.4	1.6	16.4
J1427.3−4204	…	…	…	…	…	…
J1512.7−0906	3.8*	0.14	2.5	9.7	0.0	9.7
J2000.9−1749	13.0†	0.25	6.0	13.4	0.5	15.7
J2254.0+1613	5.8*	0.09	1.9	6.2	0.0	6.9
		Elevated Activity State				
J0456.9−2323	35.3*	0.55	15.3	34.7	3.6	38.3
J0957.6+5523	…	…	…	…	…	…
J1224.7+2124	29.1*	0.99	1.8	50.8	0.0	55.3
J1256.2−0548	34.5*	0.53	20.1	33.1	3.7	37.9
J1427.3−4204	…	…	…	…	…	…
J1512.7−0906	25.8*	0.96	17.1	66.4	0.1	66.6
J2000.9−1749	…	…	…	…	…	…
J2254.0+1613	25.0*	0.41	8.7	28.0	0.2	28.4

Note. Columns are as follows: (1) 2FHL name; (2) average optical polarization taken from Steward or RoboPol observatories (marked with * and †, respectively; Smith et al. 2009; Pavlidou et al. 2014); (3) depolarization factor Z_m, as described in Section 4.3; (4) and (5) degree of polarization predicted at 1 keV from leptonic and hadronic modeling, respectively; and (6) and (7) degree of polarization predicted at 1 MeV from Leptonic and Hadronic Modeling, respectively. Note that we derive the polarization at 1 keV and 1 MeV both for the average and elevated activity states appropriately correcting for a partially ordered magnetic field. The high activity state optical polarizations are collected from the Steward observatory database.

To summarize, the current generation polarimeters are likely to detect X-ray and γ-ray polarization during active states of FSRQs for both leptonic and hadronic models, and in particular when the optical polarization degree is high. Considering the fact that FSRQs peak between MeV and GeV, a γ-ray polarimeter may more easily detect polarization. Three polarization features of FSRQs can distinguish the leptonic and hadronic models: (1) the hadronic model shows a systematic higher polarization degree than the leptonic; (2) in the hadronic model, the X-ray and γ-ray polarization degrees are similar, while in the leptonic model, the X-ray polarization is higher than γ-ray; and (3) the hadronic polarization is generally higher than the optical counterpart, while the leptonic polarization is only half of that.

6.4. A Detection beyond 50 GeV and the Gamma-Ray Absorption

In the leptonic emission framework, the origin of the γ-ray radiation in FSRQs is believed to be due to IC scattering of BLR photons by the jet electrons. However, the same BLR radiation field can also absorb γ-rays via the $\gamma\gamma$ pair production process (e.g., Donea & Protheroe 2003; Liu & Bai 2006). This is aligned with the fact that only a handful of FSRQs are detected in the VHE band.[10] Knowledge of the BLR absorption enables us to constrain the location of the γ-ray emission region by requiring that the optical depth for γ-ray absorption should be small ($\tau_{\gamma\gamma} < 1$) at $R_{\rm diss}$. Therefore, it is of great interest to study the effect of the BLR absorption on the γ-ray spectra of 2FHL FSRQs.

Recently, Böttcher & Els (2016) developed a novel approach to quantify the $\gamma\gamma$ opacity due to the BLR radiation field that primarily depends on the BLR luminosity and energy density. These parameters can be constrained from the observations: either from the emission line luminosities or from the modeling of the big blue bump (see Section 5 for details). Therefore, we adopt the methodology described in Böttcher & Els (2016) to derive $\tau_{\gamma\gamma}$ as a function of $R_{\rm diss}$. The results are shown in Figure 6. In this figure, various colored lines correspond to $\tau_{\gamma\gamma}$ as a function of $R_{\rm diss}$ derived for γ-ray photons of different energies, as labeled. The location of the γ-ray emitting region is also shown with the vertical dotted line. As can be seen, $\tau_{\gamma\gamma}$ is very small at $R_{\rm diss}$, even for a γ-ray photon of $\sim$300 GeV energy (except for J2254.0+1613 where $\tau_{\gamma\gamma} \gtrsim 1$). Interestingly, according to our calculation, the BLR is transparent to $\sim$50 GeV photon even at its inner boundary (shown with the vertical dashed line). This implies that the γ-ray emission region can be located close to the BLR where the BLR radiative energy density is dense enough to act as a primary reservoir of seed photon for the EC process, however, sufficiently transparent to high energy (50–100 GeV) γ-ray photons.

6.5. Prospects for VHE Emission and EBL Studies

A statistically significant detection above 50 GeV by *Fermi*-LAT makes blazars viable candidates for observations in the VHE band with ground-based Cherenkov telescopes such as H.E.S.S., MAGIC, and VERITAS. As of now, only seven FSRQs are known as VHE emitters and this work includes three of them, i.e., J1224.7+2124 (Aleksić et al. 2011), J1256.2−0548 (MAGIC Collaboration et al. 2008), and J1512.7−0906 (H.E.S.S. Collaboration et al. 2013).

The 2FHL spectral shapes of the FSRQs provides us with a clue about their VHE detection possibility due to the broad energy coverage of the 2FHL catalog (up to 2 TeV). In

[10] http://tevcat.uchicago.edu/

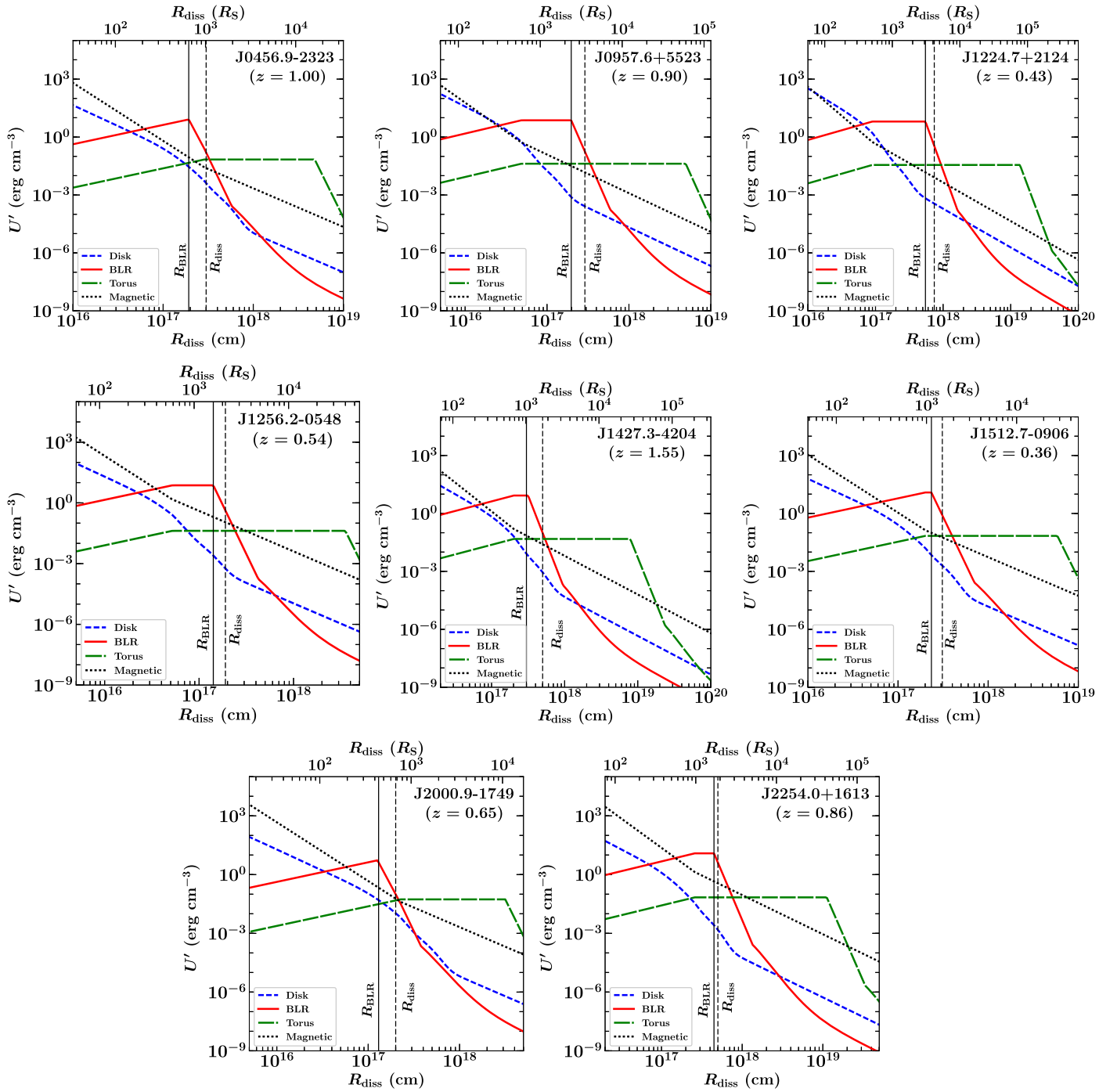

Figure 5. Dissipation distance dependence of the comoving frame radiative energy densities. Vertical black solid and dashed lines represent the inner boundary of the BLR and the location of the emission region as inferred from the leptonic SED modeling, respectively. Note that the bulk Lorentz factor Γ varies as $\min[(R_{\rm diss}/3R_{\rm S})^{1/2}, \Gamma_{\rm max}]$, i.e., an accelerating jet followed by a constant moving phase (see, Ghisellini & Tavecchio 2009).

Figure 1, where the 100 MeV−2 TeV γ-ray SEDs are shown, we overplot the sensitivity limits of the MAGIC and HESS telescopes (pink and green solid lines, respectively) and the future CTA-North and CTA-South observatories[11] (black dashed and solid lines, respectively) for an integration time of 50 hr and a given zenith angle (Holler et al. 2015; Aleksić et al. 2016). By comparing the 2FHL spectral points with CTA sensitivity curves, we expect that CTA will possibly be able to detect all of them except J1427.3−4204 and J2254.0+1613. These two objects have the two softest 2FHL spectra among all the FSRQs and there is only marginal overlap between the CTA sensitivity curve and their 2FHL bow-tie plot. For both of them, the 2FHL spectral points lie well below the CTA sensitivity plots. In fact, the 3FGL spectrum of J2254.0+1613 is modeled as a power law with an exponential cutoff (Acero et al. 2015), indicating the presence of a sharp decline in the

[11] The sensitivity limits for all instruments are extracted from the public CTA page: https://www.cta-observatory.org/science/cta-performance/#1472563157332-1ef9e83d-426c. Note that not all of the sources are visible from all of the facilities. Therefore, for positive declination sources, we show sensitivity plots of CTA-North and MAGIC, whereas, HESS and CTA-South sensitivity curves are used for southern hemisphere objects.

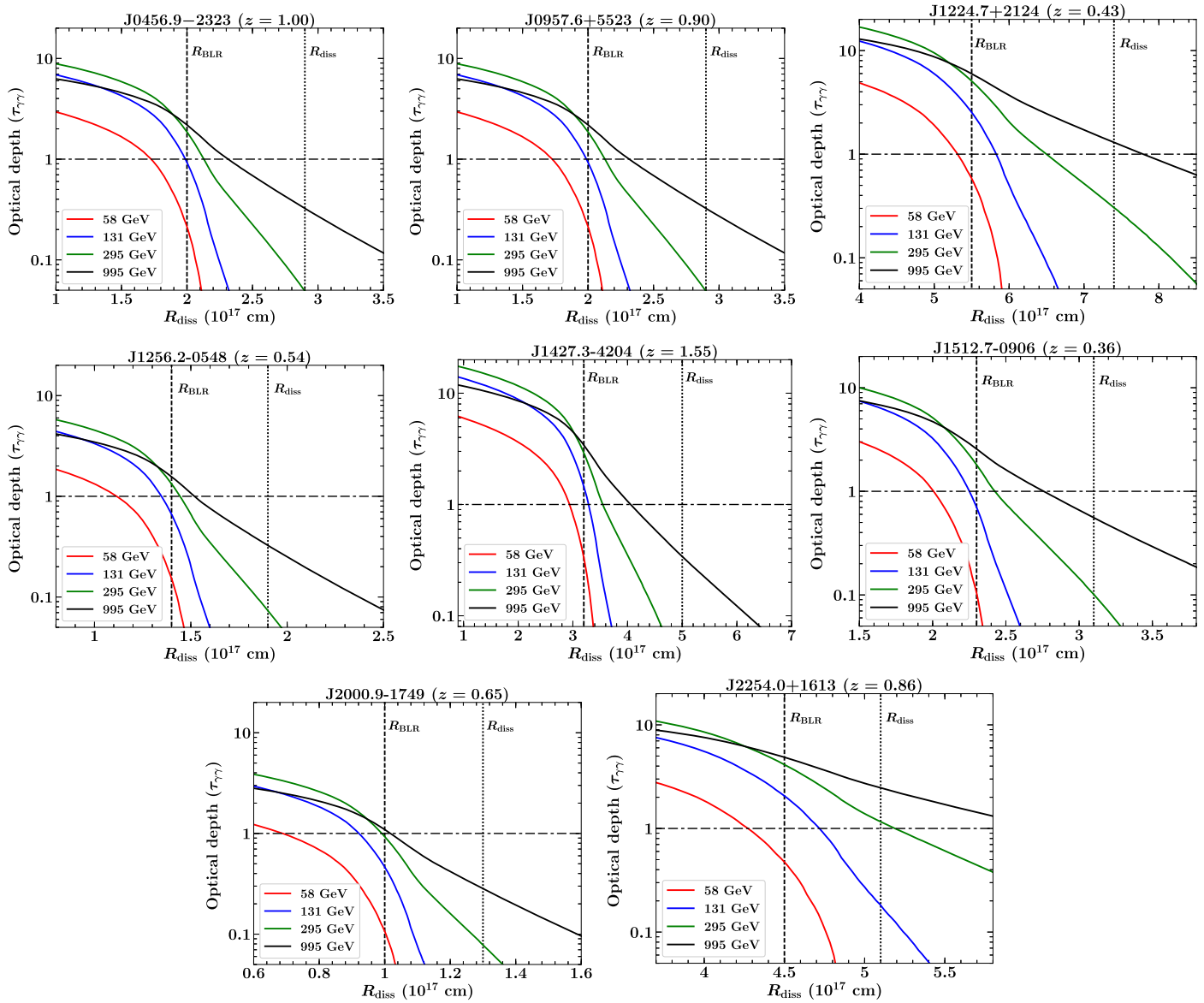

Figure 6. Variation of $\gamma\gamma$ absorption optical depth ($\tau_{\gamma\gamma}$) as a function of the location of the emission region ($R_{\rm diss}$) along the jet. Vertical black dashed and dotted lines correspond to the inner radius of the BLR and the location of the emission region, respectively, as inferred from the leptonic SED modeling. Horizontal black dashed–dashed–dotted line represents $\tau_{\gamma\gamma} = 1$. Various colored lines denote the variation of the optical depths derived for γ-ray photons of different energies, as labeled.

flux above 50 GeV. McConville et al. (2011) predicted J0957.6 +5523 as a plausible candidate for VHE detection due to its hard 0.1–300 GeV spectrum and the lack of significant γ-ray flux variability; however, a dedicated observing campaign of 35 hr with MAGIC and 45 hr from VERITAS only resulted in flux upper limits (Furniss & McConville 2013; Aleksić et al. 2014). A comparison with the MAGIC sensitivity curve in the γ-ray spectrum of J0957.6+5523 (Figure 1) suggests that the source would be difficult to detect even in 50 hr of integration. Furthermore, as of now, all the FSRQs are detected in the VHE band during flaring activity periods. However, the unprecedented sensitivity of CTA will allow us to observe these FSRQs (and many more) even during their average low activity states.

In general, EBL studies using blazars are more prone toward BL Lac objects (Domínguez & Ajello 2015). This is mainly due to the hard γ-ray spectra of these sources on which the EBL imprint can easily be observed (e.g., Ackermann et al. 2012). FSRQs, on the other hand, are rarely detected above 10−20 GeV due to their soft γ-ray spectrum. Furthermore, $\gamma\gamma$ absorption on the BLR radiation field may be difficult to disentangle from EBL absorption effects. Therefore, EBL studies with FSRQs are generally more difficult than with BL Lac sources. In this regard, 2FHL FSRQs can be used to probe the theories of the redshift dependence of EBL evolution as they are observed above 50 GeV and also they are located at high redshifts ($z > 0.5$). Furthermore, based on the $\gamma\gamma$ opacity estimation for the BLR absorption, we found $\tau_{\gamma\gamma} < 1$ at the location of the γ-ray emitting regions, thus indicating a negligible BLR absorption effect on the γ-ray spectra of 2FHL FSRQs (Figure 6). In Figure 7, we plot the energy of the highest energy photons (HEP) detected from 2FHL sources as a function of their redshifts; 2FHL FSRQs are marked with stars. We use the EBL attenuation model of Domínguez et al. (2011) to derive the EBL optical depth ($\tau_{\rm EBL}$) for all the sources (see the color scheme in Figure 7) and show the cosmic γ-ray horizon with 1σ uncertainty, as derived by this model

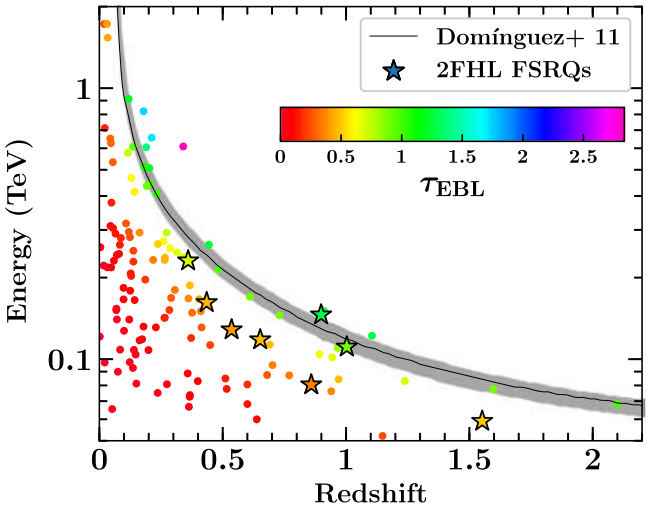

Figure 7. Plot of the energy of the highest energy photons detected from 2FHL sources vs. redshift, as reported in Ackermann et al. (2016). The 2FHL FSRQs are shown with stars. The color scheme represents the optical depth (τ_{EBL}) for a given energy and redshift following the EBL attenuation model of Domínguez et al. (2011), as shown in the colorbar. Solid black line denotes the cosmic γ-ray horizon with 1σ uncertainties (shaded area) adopting the same EBL model. As can be seen, on average, the FSRQs follow the opacity pattern expected from the EBL model.

(see also Domínguez et al. 2013). We do not see any major deviation from the predicted horizon and they are located in the more transparent region. However, there are a couple of noteworthy observations. As can be seen, the optical depth toward the FSRQ J0957.6+5523 ($z = 0.9$ and HEP $= 145$ GeV) matches the γ-ray horizon within the 1σ uncertainty of the latter. Moreover, at a redshift of 1.55, J1427.3−4204 is the most distant FSRQ in the 2FHL catalog and has the softest 2FHL spectrum in our sample. It lies well below the $\tau_{EBL} = 1$ line in Figure 7, which is consistent with its observed γ-ray spectral behavior.

7. Summary

We have performed a broadband analysis of eight FSRQs present in the 2FHL catalog. Our findings are summarized below.

1. Both leptonic and hadronic emission models reasonably explain the broadband SEDs and are marginally consistent with 2FHL spectra.
2. The location of the γ-ray emission is found to be at the outer edge of the BLR and it is consistent with our quantitative estimate of the $\gamma\gamma$ opacity for the γ-ray absorption with the BLR radiation field.
3. According to our analysis, leptonic emission models predict a significantly lower degree of high energy polarization compared to the hadronic ones.
4. In the hadronic scenario, the degrees of both X-ray and γ-ray polarization are expected to be similar, but the X-ray polarization is predicted to be higher than γ-rays if blazar jets are powered by leptonic emission mechanisms.
5. It is likely that the X-ray polarimeters (e.g., IXPE) may detect a significant degree of polarization from FSRQs during their flaring activity states. If so, it will provide supportive evidence for the hadronic origin of the observed radiation.
6. A majority of the hard γ-ray spectrum FSRQs would be detectable with the upcoming TeV facility CTA, though J2254.0+1613 may remain below the detection threshold, especially during the nonflaring states, due to a strong cutoff in its γ-ray spectra.

We are grateful to an anonymous referee for constructive criticism. The *Fermi*-LAT Collaboration acknowledges generous ongoing support from a number of agencies and institutes that have supported both the development and the operation of the LAT as well as scientific data analysis. These include the National Aeronautics and Space Administration and the Department of Energy in the United States, the Commissariat à l'Energie Atomique and the Centre National de la Recherche Scientifique/Institut National de Physique Nucléaire et de Physique des Particules in France, the Agenzia Spaziale Italiana and the Istituto Nazionale di Fisica Nucleare in Italy, the Ministry of Education, Culture, Sports, Science and Technology (MEXT), High Energy Accelerator Research Organization (KEK) and Japan Aerospace Exploration Agency (JAXA) in Japan, and the K. A. Wallenberg Foundation, the Swedish Research Council and the Swedish National Space Board in Sweden. Additional support for science analysis during the operations phase is gratefully acknowledged from the Istituto Nazionale di Astrofisica in Italy and the Centre National d'Études Spatiales in France. This research has made use of data obtained through the High Energy Astrophysics Science Archive Research Center Online Service, provided by the NASA/Goddard Space Flight Center. Part of this work is based on archival data, software, or online services provided by the ASI Data Center (ASDC). This research has made use of the XRT Data Analysis Software (XRTDAS). This work made use of data supplied by the UK Swift Science Data Centre at the University of Leicester. A.D. thanks the support of the Juan de la Cierva program from the Spanish MEC. The work of M. B. is supported by the South African Research Chair Initiative (SARChI) of the Department of Science and Technology and the National Research Foundation[12] of South Africa. H.Z. acknowledges support from Fermi Guest Investigator program Cycle 10, grant No. 80NSSC17K0753.

Software: XSPEC (Arnaud 1996), Swift-XRT data product generator (Evans et al. 2009).

ORCID iDs

Vaidehi S. Paliya https://orcid.org/0000-0001-7774-5308
Haocheng Zhang https://orcid.org/0000-0001-9826-1759
Markus Böttcher https://orcid.org/0000-0002-0455-3791
M. Ajello https://orcid.org/0000-0002-6584-1703
A. Domínguez https://orcid.org/0000-0002-3433-4610
M. Joshi https://orcid.org/0000-0003-1134-7352
D. Hartmann https://orcid.org/0000-0002-8028-0991
C. S. Stalin https://orcid.org/0000-0002-4998-1861

References

Abdo, A. A., Ackermann, M., Agudo, I., et al. 2010, ApJ, 716, 30
Abdo, A. A., Ackermann, M., Ajello, M., et al. 2011, ApJ, 736, 131
Acero, F., Ackermann, M., Ajello, M., et al. 2015, ApJS, 218, 23
Ackermann, M., Ajello, M., Allafort, A., et al. 2012, Sci, 338, 1190

[12] Any opinion, finding, and conclusion or recommendation expressed in this material is that of the authors and the NRF does not accept any liability in this regard.

Ackermann, M., Ajello, M., Allafort, A., et al. 2013, ApJS, 209, 34
Ackermann, M., Ajello, M., Atwood, W. B., et al. 2015, ApJ, 810, 14
Ackermann, M., Ajello, M., Atwood, W. B., et al. 2016, ApJS, 222, 5
Aharonian, F. A. 2000, NewA, 5, 377
Ajello, M., Atwood, W. B., Baldini, L., et al. 2017, ApJS, 232, 18
Aleksić, J., Ansoldi, S., Antonelli, L. A., et al. 2014, MNRAS, 440, 530
Aleksić, J., Ansoldi, S., Antonelli, L. A., et al. 2016, APh, 72, 76
Aleksić, J., Antonelli, L. A., Antoranz, P., et al. 2011, ApJL, 730, L8
Arnaud, K. A. 1996, in ASP Conf. Ser. 101, Astronomical Data Analysis Software and Systems V, ed. G. H. Jacoby & J. Barnes (San Francisco, CA: ASP), 17
Atwood, W., Albert, A., Baldini, L., et al. 2013, arXiv:1303.3514
Barnacka, A., Geller, M. J., Dell'Antonio, I. P., & Zitrin, A. 2016, ApJ, 821, 58
Begelman, M. C., & Sikora, M. 1987, ApJ, 322, 650
Bonnoli, G., Ghisellini, G., Foschini, L., Tavecchio, F., & Ghirlanda, G. 2011, MNRAS, 410, 368
Bonometto, S., & Saggion, A. 1973, A&A, 23, 9
Böttcher, M., & Els, P. 2016, ApJ, 821, 102
Böttcher, M., Reimer, A., Sweeney, K., & Prakash, A. 2013, ApJ, 768, 54
Breeveld, A. A., Landsman, W., Holland, S. T., et al. 2011, in AIP Conf. Ser. 1358, ed. J. E. McEnery, J. L. Racusin, & N. Gehrels (Melville, NY: AIP), 373
Burrows, D. N., Hill, J. E., Nousek, J. A., et al. 2005, SSRv, 120, 165
Celotti, A., & Ghisellini, G. 2008, MNRAS, 385, 283
Celotti, A., Padovani, P., & Ghisellini, G. 1997, MNRAS, 286, 415
Cerruti, M., Dermer, C. D., Lott, B., Boisson, C., & Zech, A. 2013, ApJL, 771, L4
Dai, H., Xie, G. Z., Zhou, S. B., et al. 2007, AJ, 133, 2187
Dermer, C. D. 1995, ApJL, 446, L63
Dermer, C. D., Cerruti, M., Lott, B., Boisson, C., & Zech, A. 2014, ApJ, 782, 82
Domínguez, A., & Ajello, M. 2015, ApJL, 813, L34
Domínguez, A., Finke, J. D., Prada, F., et al. 2013, ApJ, 770, 77
Domínguez, A., Primack, J. R., Rosario, D. J., et al. 2011, MNRAS, 410, 2556
Donea, A.-C., & Protheroe, R. J. 2003, APh, 18, 377
Evans, P. A., Beardmore, A. P., Page, K. L., et al. 2009, MNRAS, 397, 1177
Falomo, R., Treves, A., Scarpa, R., Paiano, S., & Landoni, M. 2017, MNRAS, 470, 2814
Francis, P. J., Hewett, P. C., Foltz, C. B., et al. 1991, ApJ, 373, 465
Frank, J., King, A., & Raine, D. J. 2002, Accretion Power in Astrophysics (Cambridge: Cambridge Univ. Press), 398
Furniss, A., & McConville, W. 2013, arXiv:1303.1103
Ghisellini, G., & Tavecchio, F. 2009, MNRAS, 397, 985
Ghisellini, G., Tavecchio, F., Maraschi, L., Celotti, A., & Sbarrato, T. 2014, Natur, 515, 376
Guo, F., Li, X., Li, H., et al. 2016, ApJL, 818, L9
Hauser, M. G., & Dwek, E. 2001, ARA&A, 39, 249
Hervet, O., Boisson, C., & Sol, H. 2016, A&A, 592, A22
H.E.S.S. Collaboration, Abramowski, A., Acero, F., et al. 2013, A&A, 554, A107
Holler, M., de Naurois, M., Zaborov, D., Balzer, A., & Chalmé-Calvet, R. 2015, ICRC (The Hague), 34, 980
Janiak, M., Sikora, M., & Moderski, R. 2015, MNRAS, 449, 431
Jorstad, S. G., Marscher, A. P., Lister, M. L., et al. 2005, AJ, 130, 1418
Joshi, M., Marscher, A. P., & Böttcher, M. 2014, ApJ, 785, 132
Kalberla, P. M. W., Burton, W. B., Hartmann, D., et al. 2005, A&A, 440, 775
Kapanadze, B., Dorner, D., Romano, P., et al. 2017, ApJ, 848, 103
Lister, M. L., Aller, M. F., Aller, H. D., et al. 2013, AJ, 146, 120
Liu, H. T., & Bai, J. M. 2006, ApJ, 653, 1089
Madejski, G. M., Nalewajko, K., Madsen, K. K., et al. 2016, ApJ, 831, 142
MAGIC Collaboration, Albert, J., Aliu, E., et al. 2008, Sci, 320, 1752
Mannheim, K., & Biermann, P. L. 1992, A&A, 253, L21
Marscher, A. P. 2014, ApJ, 780, 87
Marscher, A. P., & Gear, W. K. 1985, ApJ, 298, 114
McConville, W., Ostorero, L., Moderski, R., et al. 2011, ApJ, 738, 148
Mücke, A., & Protheroe, R. J. 2001, APh, 15, 121
Oke, J. B., Shields, G. A., & Korycansky, D. G. 1984, ApJ, 277, 64
Paliya, V. S., Marcotulli, L., Ajello, M., et al. 2017, ApJ, 851, 33
Paliya, V. S., Sahayanathan, S., & Stalin, C. S. 2015, ApJ, 803, 15
Pavlidou, V., Angelakis, E., Myserlis, I., et al. 2014, MNRAS, 442, 1693
Pian, E., Urry, C. M., Maraschi, L., et al. 1999, ApJ, 521, 112
Pjanka, P., Zdziarski, A. A., & Sikora, M. 2017, MNRAS, 465, 3506
Planck Collaboration, Ade, P. A. R., Aghanim, N., et al. 2016, A&A, 594, A13
Poutanen, J., & Stern, B. 2010, ApJL, 717, L118
Roming, P. W. A., Kennedy, T. E., Mason, K. O., et al. 2005, SSRv, 120, 95
Rybicki, G. B., & Lightman, A. P. 1985, Radiative Processes in Astrophysics (New York: Wiley)
Sbarrato, T., Ghisellini, G., Maraschi, L., & Colpi, M. 2012, MNRAS, 421, 1764
Schlafly, E. F., & Finkbeiner, D. P. 2011, ApJ, 737, 103
Shakura, N. I., & Sunyaev, R. A. 1973, A&A, 24, 337
Shaw, M. S., Romani, R. W., Cotter, G., et al. 2012, ApJ, 748, 49
Sikora, M., Rutkowski, M., & Begelman, M. C. 2016, MNRAS, 457, 1352
Sironi, L., & Spitkovsky, A. 2011, ApJ, 726, 75
Smith, P. S., Montiel, E., Rightley, S., et al. 2009, arXiv:0912.3621
Stickel, M., Fried, J. W., & Kuehr, H. 1989, A&AS, 80, 103
Stickel, M., & Kuehr, H. 1993, A&AS, 100, 395
Tavecchio, F., Becerra-Gonzalez, J., Ghisellini, G., et al. 2011, A&A, 534, A86
Urry, C. M., & Padovani, P. 1995, PASP, 107, 803
Weisskopf, M. C., Ramsey, B., O'Dell, S., et al. 2016, Proc. SPIE, 9905, 990517
Woo, J.-H., & Urry, C. M. 2002, ApJ, 579, 530
Zdziarski, A. A., & Böttcher, M. 2015, MNRAS, 450, L21
Zhang, H., & Böttcher, M. 2013, ApJ, 774, 18
Zhang, H., Chen, X., Böttcher, M., Guo, F., & Li, H. 2015, ApJ, 804, 58
Zhang, H., Diltz, C., & Böttcher, M. 2016, ApJ, 829, 69